Published in final edited form as:
Int J Hyperthermia. 2013 November ; 29(7): 629–642. doi:10.3109/02656736.2013.841327.

Approaches for modeling interstitial ultrasound ablation of tumors within or adjacent to bone: Theoretical and experimental evaluations

Serena J. Scott[a,b], **Punit Prakash**[c], **Vasant Salgaonkar**[a], **Peter D. Jones**[a], **Richard N. Cam**[a], **Misung Han**[d], **Viola Rieke**[d], **E. Clif Burdette**[e], and **Chris J. Diederich**[a,b]

[a]Thermal Therapy Research Group, Department of Radiation Oncology, University of California, San Francisco, California, USA

[b]UC Berkeley – UC San Francisco Graduate Program in Bioengineering, California, USA

[c]Department of Electrical and Computer Engineering, Kansas State University, Manhattan, Kansas, USA

[d]Department of Radiology and Biomedical Imaging, University of California, San Francisco, California, USA

[e]Acoustic MedSystems, Savoy, Illinois, USA

Abstract

Purpose—The objectives of this study were to develop numerical models of interstitial ultrasound ablation of tumors within or adjacent to bone, to evaluate model performance through theoretical analysis, and to validate the models and approximations used through comparison to experiments.

Methods—3D transient biothermal and acoustic finite element models were developed, employing four approximations of 7 MHz ultrasound propagation at bone/soft tissue interfaces. The various approximations considered or excluded reflection, refraction, angle-dependence of transmission coefficients, shear mode conversion, and volumetric heat deposition. Simulations were performed for parametric and comparative studies. Experiments within *ex vivo* tissues and phantoms were performed to validate the models by comparison to simulations. Temperature measurements were conducted using needle thermocouples or MR temperature imaging (MRTI). Finite element models representing heterogeneous tissue geometries were created based on segmented MR images.

Results—High ultrasound absorption at bone/soft tissue interfaces increased the volumes of target tissue that could be ablated. Models using simplified approximations produced temperature profiles closely matching both more comprehensive models and experimental results, with good agreement between 3D calculations and MRTI. The correlation coefficients between simulated

---

Correspondence: Chris J. Diederich, PhD, Thermal Therapy Research Group, University of California, San Francisco, 1600 Divisadero Street, Suite H1031, San Francisco, CA 94143-1708. Tel: (415) 476-8641. Fax (415) 353-9883. cdiederich@radonc.ucsf.edu.

Declarations of interest
The authors alone are responsible for the content and writing of the paper.

and measured temperature profiles in phantoms ranged from 0.852 to 0.967 (p-value < 0.01) for the four models.

Conclusions—Models using approximations of interstitial ultrasound energy deposition around bone/soft tissue interfaces produced temperature distributions in close agreement with comprehensive simulations and experimental measurements. These models may be applied to accurately predict temperatures produced by interstitial ultrasound ablation of tumors near and within bone, with applications toward treatment planning.

Keywords

Interstitial ultrasound; thermal ablation; bone; theoretical model

Introduction

Primary and metastatic bone tumors remain a significant clinical problem for local control and pain palliation. Bone metastases are highly prevalent, observed upon autopsy in 65-75% of breast and prostate cancer patients [1, 2], while primary bone tumors are far less common [3]. Because patients with bone metastases have poor prognoses, the aims of metastatic bone tumor treatment are usually directed toward local control or palliation [4-6]. The goals of palliative bone cancer treatment are to relieve pain and to maintain or restore mechanical stability and neurological function [4-7]. Bone tumors are generally treated with surgery, radiation, and/or chemotherapy [5-8]. External beam radiation is currently the standard of care for relief of pain caused by bone metastases [5, 6, 9]. Thermal ablation has previously been investigated for the treatment of primary bone tumors and for palliative treatment of metastases [9-19]. Tumors within or adjacent to bone can be treated externally using focused ultrasound ablation (FUS) [14-16] or percutaneously with radiofrequency (RF) ablation [11-13], microwave (MW) ablation [17], laser ablation [18], or cryoablation [19]. RF ablation is the most widely used, and a common treatment for osteoid osteoma [9]. Externally applied FUS has gained attention in recent years, but it requires an acoustic window to access the bone and it targets the bone surface with little penetration through intact cortical shell [14-16].

We are investigating the use of interstitial ultrasound as an alternative percutaneous ablation modality for the treatment of tumors within and near bone. Interstitial ultrasound applicators provide an energy delivery platform that utilizes tubular acoustic radiators within a water-cooled catheter [20, 21]. Multiple independently powered tubular transducers can be positioned along the length of an applicator and sectored longitudinally to allow for directional heating control along the applicator’s length and angular expanse. These devices are designed for percutaneous placement inside or adjacent to a target. They can generate well-localized thermal lesions at 15 – 21 mm radial depth within 5 – 10 min with heat deposition tailored to target shapes, producing excellent spatial control compared to RF ablation, MW ablation, laser ablation, and cryotherapy [22-24]. The impact of bone, either surrounding or adjacent to a soft tissue tumor, on thermal ablation with this modality has not been well defined; it will be a critical component in understanding the performance of interstitial ultrasound ablation of targets involving bone, providing the motivation of this study.

Reflection, refraction, and shear mode conversion play significant roles in ultrasound wave propagation at bone/soft tissue interfaces, making bone surfaces much more complex to acoustically model than soft tissue interfaces. Shear wave transmission in fluids and soft tissues is negligible, but at incidence angles above about 27°, the majority of the acoustic energy transmitted into bone is converted to shear waves [25, 26]. Furthermore, the high ultrasound attenuation coefficient of bone, over an order of magnitude higher than that of most soft tissues [27], results in considerable heating at bone surfaces when ultrasound is applied [25, 28].

Acoustic simulations in bone have been employed in the past to correlate acoustic properties of bone to structural properties and disease states [29, 30], and to study intended and unintended bone heating during ultrasound imaging and thermal therapy [25, 31-34]. Previous studies have taken a variety of approaches to modeling ultrasound propagation in and near bone.

Some studies modeled shear [35] and longitudinal waves [34, 35] with an exponential intensity falloff, others calculated the full stress tensor, with shear and longitudinal components, in bone as a function of incidence angle [26], and others did not consider shear mode conversion, which allowed easier implementation of full wave methods [31] or the Rayleigh-Sommerfeld diffraction integral [32, 36, 37] to simulate propagation through the interface. Recent studies investigated bone heating with planar, curvilinear, and cylindrical transurethral ultrasound transducers [32, 33]. They applied numerical models with constant transmission coefficients independent of incidence angle and did not consider reflection [32, 33]. However, many prior acoustic and thermal simulations of ultrasound near bone have been performed with either planar transducers [32, 34, 37, 38], assuming low incidence angles and purely longitudinal transmission [34, 38], or focused [25, 31, 35, 36, 39] transducers.

The objective of this study is to develop 3D transient biothermal and acoustic models specific to interstitial ultrasound ablation of tumors within or adjacent to bone. Different approaches for approximating ultrasound propagation at bone/soft tissue interfaces are developed and incorporated into the models. The models are appraised and validated by parametric studies, comparison with one another, and comparison to heating experiments. Thermocouple and MR-based thermometry are used in *ex vivo* tissue and phantom experiments to obtain transient temperature distributions for comparison with numerical predictions. The theoretical models developed in this study provide quantitative assessment of interstitial ultrasound ablation of tumors in and near bone, and can be applied to treatment planning.

Materials and Methods

THEORY

Finite element analysis of heat transfer—In order to investigate the effects of bone on acoustic propagation, temperature distributions, and thermal dose distributions during interstitial ultrasound ablation, 3D finite-element models were developed based on the Pennes bioheat transfer equation [40]:

$$\rho c\frac{dT}{dt}=\nabla\cdot \mathrm{k}\nabla \mathrm{T}-\omega \mathrm{c_b}\left(T-T_b\right)+Q \quad (1)$$

where ρ is density (kg/m^3), c is specific heat capacity (J/kg/°C), T is temperature (°C), t is time (s), k is thermal conductivity (W/m/°C), ω is blood perfusion (kg/m^3/s), Q is heat deposition due to ultrasound (W/m^3), and the subscript b refers to blood. Capillary blood temperature is assumed to be 37°C. Dynamic changes in perfusion due to coagulation are incorporated into models of *in vivo* ablations. To simulate the effect of heating-induced microvascular stasis, perfusion is reduced to zero at a thermal dose threshold of 300 cumulative equivalent minutes at 43°C (CEM43°C) [41], with thermal dose calculated according to Sapareto and Dewey [42]. The tissue and material properties used in this study are summarized in Table I.

Catheter-cooled ultrasound applicators consisted of an array of two cylindrical transducers, each 1.5 mm outer diameter (OD) and 10 mm long (L), sonicating at 6.9-7.5 MHz from within a plastic implant catheter (2.4 mm OD, 1.89 mm inner diameter (ID)) with integrated water-cooling (Figure 1A). The acoustic power deposition Q (W/m^3) from these cylindrical radiators can be described as a longitudinally collimated and radially diverging intensity pattern (I) [43, 44].

$$Q=2\alpha I=2\alpha I_s\frac{r_t}{r}e^{-2\int_{r_t}^{r}\mu dr'} \quad (2)$$

where α is the ultrasound absorption coefficient (Np/m), I_s is the acoustic intensity on the transducer surface (W/m), r_t is the transducer radius (m), r is the radial distance from the transducer's central axis (m), and μ is the ultrasound attenuation coefficient (Np/m). The absorption coefficient is assumed to be equivalent to the attenuation coefficient, with scattered energy locally absorbed. The attenuation of the catheter wall was modeled as 43.9 Np/m/MHz [45].

Finite element analysis was performed using COMSOL Multiphysics 4.3 with MATLAB to generate transient temperature and thermal dose distributions for various model configurations and to model experimental studies within *ex vivo* tissues and phantoms. Simulations were performed on an Intel Xeon X5680 processor, with 6 cores each operating at 3.33 GHz on a Rad Hat Linux operating system. The catheter was modeled as a 1.89 mm ID and 2.4 mm OD cylinder, with a maximum mesh size of 0.4 mm on its inner surface. The ultrasound source was modeled as two cylinders (1.5 mm OD, 1 cm L) within the catheter. The maximum mesh size on the outermost boundaries of the geometry was 5 mm, and the maximum mesh size on heated bone surfaces was 0.3-1 mm, with finer bone meshes used when the applicator was closer to the bone surface. The mesh size in the soft tissue between the applicator and the bone was limited to a maximum of 0.7-2.5 mm, depending on the distance between the catheter and bone surfaces. Convergence tests were performed to ensure that all mesh sizes on the bone, near the applicator, and on outer boundaries were sufficiently fine for a stable solution. The initial temperature was set to 22 or 37°C, depending on whether the simulation was performed to model bench top or physiological conditions. An implicit transient solver with a variable time step taken at least once in each

10 second time span was used to solve the transient bioheat equation. The maximum step size for thermal dose calculations was 10-20 seconds. Fixed temperature boundary conditions (equal to the initial temperature) were applied at the outermost boundaries of the geometry. A convective boundary condition was imposed on the inner surface of the catheter, with a heat transfer coefficient h = 1000 W/m^2/°C [46, 47] and flow temperature T_f = 22°C.

$$-\hat{\boldsymbol{n}}\cdot(-k\nabla \mathrm{T})=h\left(T_f-T\right) \quad (3)$$

where $\hat{\boldsymbol{n}}$ is the normal unit vector to the boundary.

Interactions at bone/soft tissue interfaces—When an acoustic wave travelling through soft tissue hits a cortical bone surface, a significant portion of the energy is reflected due to an impedance mismatch. At normal incidence, the remaining energy is transmitted as longitudinal waves. If the incident angle is not normal, some or all of the transmitted energy is converted to shear waves, and both longitudinal and shear waves are refracted (Figure 2). Defining θ as the angle between the direction in which the wave travels and the normal of the bone surface, the reflection and refraction angles can be defined by Snell's Law, with the reflection and transmission coefficients defined [48] as

$$R\equiv\frac{I_r}{I_i}=\left|\frac{Z_L cos^2\left(2\theta_s\right)+Z_s\quad sin^2\left(2\theta_s\right)-Z_1}{Z_L cos^2\left(2\theta_s\right)+Z_s sin^2\left(2\theta_s\right)+Z_1}\right|^2 \quad (4)$$

$$\mathscr{T}_L\equiv\frac{I_L}{I_i}=\frac{\rho_2\quad tan\quad\theta_i}{\rho_1\quad tan\quad\theta_L}\left|\frac{2\rho_1 Z_L cos\left(2\theta_s\right)}{\rho_2\left(Z_L cos^2\left(2\theta_s\right)+Z_s sin^2\left(2\theta_s\right)+Z_1\right)}\right|^2 \quad (5)$$

$$\mathscr{T}_s\equiv\frac{I_s}{I_i}=\frac{\rho_2\quad tan\quad\theta_i}{\rho_1\quad tan\quad\theta_s}\left|\frac{2\rho_1 Z_s sin\left(2\theta_s\right)}{\rho_2\left(Z_L cos^2\left(2\theta_s\right)+Z_s sin^2\left(2\theta_s\right)+Z_1\right)}\right|^2 \quad (6)$$

$$Z_1=\frac{\rho_1\nu_1}{cos\quad\theta_i} \quad (7)$$

$$Z_L=\frac{\rho_2\nu_L}{cos\quad\theta_L} \quad (8)$$

$$Z_s=\frac{\rho_2\nu_s}{cos\quad\theta_s} \quad (9)$$

where r is the reflection coefficient, $\mathscr{T}$ is the transmission coefficient, I is intensity (W/m^2), ν is the speed of sound (m/s), subscript 1 refers to soft tissue, subscript 2 refers to bone, subscript i refers to the incident wave, subscript r refers to the reflected wave, subscript L refers to the longitudinal wave in bone, and subscript s refers to the shear wave in bone.

In contrast, specular reflection and transmission cannot be assumed in cases when cancellous bone is in direct contact with an osteolytic tumor without a smooth cortical shell in between the bone surface and the transducer. The incidence angle on the sponge-like bony trabeculae within cancellous bone is different from the incidence angle on the bulk tissue as a whole. Thus, we assume that 10% of the energy incident on cancellous bone is reflected and 90% is transmitted and locally absorbed, regardless of incidence angle [49, 50].

In order to determine what approximations can accurately represent interstitial ultrasound heating at a bone/soft tissue interface, a series of models of decreasing complexity were developed (summarized in Table II). These simplified models were devised to investigate the relative impacts of reflection, refraction, mode conversion, and heating throughout the bone volume on predicted temperatures and thermal lesion sizes.

Model A - Angle-dependent volumetric—The angle-dependent volumetric model, Model A, considers reflection, refraction, and shear mode conversion at cortical bone interfaces. To describe heating within and adjacent to the bone, the equations describing acoustic power deposition were multiplied by the appropriate transmission and reflection coefficients, as in Moros et al. and Lin et al. [34, 35]:

$$Q_1^A = Q_{1,i} + Q_{1,r} = 2\alpha I_s \frac{r_t}{r} e^{-2\int_{r_t}^{r} \mu dr'} + 2R\alpha I_s \frac{r_t}{r_r} e^{-2\int_{r_t}^{r_r} \mu dr'} \quad (10)$$

$$Q_2^A = Q_{2,L}^A + Q_{2,s}^A = 2\mathscr{T}_L \alpha_L I_s \frac{r_t}{r} e^{-2\left(\int_{r_t}^{r_1} \mu dr' + \int_{r_1}^{r} \mu_L dr'\right)} + 2\mathscr{T}_s \alpha_s I_s \frac{r_t}{r} e^{-2\left(\int_{r_t}^{r_1} \mu dr' + \int_{r_1}^{r} \mu_s dr'\right)} \quad (11)$$

where $r_r - r_t$ is the distance the reflected wave travels through soft tissue from the surface of the transducer and r_1 is the radial distance from the transducer center to the point where the wave crosses the bone surface. Q_1^A, the heat deposition in soft tissue in Model A, contains contributions from the incident and reflected waves. Q_2^A, the heat deposition in bone in Model A, contains contributions from the longitudinal and shear waves. This approximation directly calculates the acoustic intensity within bone, without the need to evaluate the full stress tensor.

Model B - Constant transmission volumetric—In Model B, the constant transmission volumetric model, a constant attenuation coefficient and a constant transmission coefficient, both independent of incident angle, were used in bone. Reflection and refraction were not considered. Transmitted energy is assumed to be absorbed so close to the bone surface that refraction has little effect, and the heating contributions of reflected energy are assumed to be insignificant compared to heating from the incident and transmitted waves within the highly absorbing bone. The transmission coefficient ($\mathscr{T}_I$) is calculated for normal incidence on a composite bone. Here,

$$\mathscr{T}_I \equiv \frac{I_2}{I_i} = \frac{4\rho_1\nu_1\rho_2\nu_2}{(\rho_1\nu_1 + \rho_2\nu_2)^2} = 77.3\% \quad (12)$$

$$Q_1^B = Q_{1,i} = 2\alpha I_s \frac{r_t}{r} e^{-2\int_{r_t}^{r} \mu dr'} \quad (13)$$

$$Q_2^B = 2\mathscr{T}_I \alpha I_s \frac{r_t}{r} e^{-2\int_{r_t}^{r} \mu dr'} \quad (14)$$

Model C - Angle-dependent boundary and Model D - Constant transmission boundary—Models C and D are based upon similar equations as Models A and B, respectively, but instead of volumetric power deposition within bone, all energy is assumed to be absorbed at the bone surface without penetration into the bone. Bone heating is modeled as an energy (q) applied to the bone surface as a power flux (W/m^2) equal to the intensity on the bone surface multiplied by a transmission coefficient. The assumption is that all transmitted energy (shear and longitudinal) is absorbed within such close proximity of the bone surface that the energy may be approximated as absorbed on the bone surface. Reflection was not considered and refraction is not applicable, as this approximation assumes that the energy does not penetrate any distance into the bone.

$$q = -\overrightarrow{n} \cdot (-k\nabla \mathrm{T}) \quad (15)$$

$$Q_1^C = Q_1^D = Q_{1,i} = 2\alpha I_s \frac{r_t}{r} e^{-2\int_{r_t}^{r} \mu dr'} \quad (16)$$

$$q_2^c = (\mathscr{T}_L cos \quad \theta_L + \mathscr{T}_s \quad cos \quad \theta_s) \, I_s \frac{r_t}{r} e^{-2\int_{r_t}^{r_1} \mu dr'} \quad (17)$$

$$q_2^D = \mathscr{T}_I \quad cos \quad \theta_I I_s \frac{r_t}{r} e^{-2\int_{r_t}^{r_1} \mu dr'} \quad (18)$$

$\overrightarrow{n}$ is the unit vector normal to the bone surface. The cosine terms in Eq. 17-18 define the normal component of the energy flux through the bone surface. The transmitted angle in Model D (θ_1) is the same as the incidence angle (θ_i).

The transmission and reflection coefficients in the angle-dependent models, A and C, require separate shear and longitudinal components, so these two models are calculated using the acoustic properties of cortical bone. All other properties for Models A-D are those of whole composite bones.

Comparison of models in perfused tissue—The four models were first compared in simulations of perfused tissues, with an initial temperature of 37 °C. The applicator was positioned in a block of muscle with its axis parallel to a flat bone and 10 or 20 mm away from it, as in Figure 1B. A 6.9 MHz applicator, with two transducers sectored longitudinally to produce acoustic energy in a 180° angular expanse and powered at 9.4 acoustic W/cm^2, was modeled. The initial temperature was set to 37°, and perfusion was considered. For each model, identical transient solvers (geometric multigrid) and meshing parameters were used.

Parametric investigations—To investigate these models and the effects of varying tumor properties, a 7 MHz applicator with a 135° active acoustic zone and 2 transducers was modeled in soft tissue next to a plane of composite bone, as in Figure 1B. The largest tumor that could be ablated within 10 minutes for various tumor attenuation coefficients and perfusion rates was determined. The tumor attenuation was varied from 3 to 15 Np/m/MHz, representing a range of soft tissue neoplasms [27]. Tumor perfusion was varied from 0 to 13 $kg/m^3/s$, representing zero perfusion in necrotic tumors to the high perfusion observed in some tumors [51, 52]. All other tumor properties were set to those of muscle. The target was considered fully ablated when 99% of the area between the catheter and the bone surface, ranging from 1 mm below the upper transducer's upper edge to 1 mm above the lower transducer's lower edge, exceeded 240 CEM43°C, which is considered a lethal thermal dose [53]. A proportional integral controller ($k_p = 0.2$, $k_i = 0.0017$) was implemented to modulate the power supplied to the transducers (limited to a range of 0-21.2 W/cm^2 acoustic) in order to approach and maintain a peak temperature of 85°C. 10 minute ablations using the constant transmission volumetric model were simulated. For low and high attenuations, Models A, C, and D were also applied.

EXPERIMENTS

Ex vivo *tissue ablation*—A benchtop experimental setup, including *ex vivo* porcine loin muscle and bovine bones (store bought), was developed to investigate the impact of bone on thermal ablation with interstitial ultrasound (See Figure 3A). Bovine rib and cervical vertebrae were cleaned of soft tissue, and the vertebrae were sectioned to produce a flat slab of cancellous bone from the center of the vertebrae. The bones and porcine loin muscle were degassed, allowed to equilibrate to 37°C in a water bath, and positioned adjacent to one another in a template in the bath. A catheter-cooled 6.9 MHz ultrasound applicator with two 135° transducers was inserted through the plastic template into the muscle 5-35 mm away from and parallel to an adjacent bone surface (Figure 3A). Acoustic energy (11.1, 12.5, or 22.2 W/cm^2) was applied for a 10 minute ablation. 18 ablations incorporating rib bones and 11 ablations incorporating vertebral bones were performed, with a separate portion of the muscle and bone tissues ablated in each trial. The soft tissue was then cut through the center of the ablation zone and the dimensions of gross tissue discoloration (coagulation) were measured.

Simulations of three trials with the tissue heated at 12.5 acoustic W/cm^2 were performed using Models A-D, the geometry of Figure 1B, and parameters mimicking the experimental conditions with the applicator positioned 15, 20, and 32 mm away from the bone. The simulated size and shape of thermal lesions, defined as cross-sectional area of the 52°C contour [54], were compared to the measured lesions described above.

Phantom studies with invasive thermometry—To quantify the temperatures attained during interstitial ultrasound ablation involving bone, experiments were performed in soft tissue equivalent gel phantoms with embedded bones. Store bought bovine rib (representing cortical bone) and bovine cervical vertebrae were boiled and cleaned of soft tissue. The vertebrae were sectioned to produce a flat slab of cancellous bone, and then all bones were degassed under a vacuum. Two 22 G needles were inserted into holes predrilled through the bones, holding them with their flat surfaces upright. A tissue-mimicking phantom [55] designed for ultrasound ablation, with stable acoustic and thermal properties, was poured around the bones and allowed to solidify. A multi-junction thermocouple (5 junctions, spaced every 5 mm) was placed inside one of the needles to measure the temperature in the phantom and the bone. An interstitial ultrasound applicator (6.9-7.3 MHz, 135°) within a catheter was inserted through a template into the phantom 30 mm in front of the bone, with the center of one transducer adjacent to the thermocouple (Figure 3B). At 10 minutes into the heating, the thermocouple was repositioned in increments within the needle to 6-8 locations to record a detailed temperature profile at up to 40 points spaced 0-5 mm apart. After the phantom cooled to ambient temperatures, the process was repeated to measure temperature profiles with the center of the applicator 25, 20, 15, 10, and 5 mm from the bone surface, in that order. Temperature profiles at each applicator location were obtained in 3-4 phantoms with an embedded rib bone and 3-4 phantoms with an embedded vertebral bone, for 40 ablation experiments total.

The heating of the phantoms was simulated using the geometry in Figure 1B, with sonication of 135° active sectors at 6.9 MHz and 16.6 acoustic W/cm^2. The ribs were modeled as composite bone, and the cervical bones as cancellous bone. Simulated and experimental temperature profiles were compared.

***MR temperature imaging:* Ex vivo *bone and soft tissue*—**Bovine rib and vertebrae with surrounding soft tissues (n=2) were heated with interstitial ultrasound and monitored with MR temperature imaging. The *ex vivo* tissues, previously degassed and equilibrated to room temperature, were placed inside a birdcage transmit/receive head coil in a 3T MR scanner (GE Healthcare, Waukesha, WI). A 7.45 MHz MR compatible interstitial ultrasound applicator with 180° active acoustic sectors was inserted into muscle, 5-10 mm from the irregular cortical bone surfaces, with the active sectors facing the bones. The tissues were heated with applied power levels of 9.1-10.2 acoustic W/cm^2 for 10 minutes. MRTI was performed during heating, using a 2D fast spoiled gradient echo sequence with TE = 8 ms, TR = 120 ms, flip angle = 30°, rib field of view = 12×12 cm^2, and vertebra field of view = 14×14 cm^2 in eight slices that were 5 mm thick and perpendicular to the applicator axis. The shift in the proton resonance frequency (PRF) of water, via phase mapping, was used to calculate temperature [56]. As commonly applied with this approach, phase unwrapping of the complex MR signal was performed to correct jumps in the phase changes from $-\pi$ to π [57].

3D models of the *ex vivo* rib and vertebrae ablations monitored with MRTI were developed. The Mimics Innovation Suite (Materialise NV, Leuven, Belguim) was used to manually segment MR images acquired before each ablation and to create finite element method (FEM) meshes specific to the tissue geometry. To create FEM meshes, the segmented 3D images were converted to 3D objects represented by triangular surface meshes and smoothed. A cylinder with a diameter of 1.89 mm was added to the geometry to represent the cooled inner surface of the catheter. All the surface meshes were refined to be within the size ranges used in this study (0.3-5 mm, with finer meshes where more acoustic energy is deposited), and combined into a single surface mesh of the volume. The surface mesh was then converted to a volume mesh and imported into Comsol.

The spatial distribution of heat deposition in tissue (Q) was calculated in MATLAB and imported into Comsol. First, the ultrasound attenuation coefficients throughout the volume, as defined in Comsol, were imported into MATLAB. MATLAB was then used to integrate the acoustic attenuation over a fine spatial resolution, calculate the transmission coefficients, and determine the acoustic heat deposition on the finite element grid. In contrast, heat deposition in volumes composed of rectangular prisms to model tissue and cylinders to model ultrasound applicators (Figure 1B) was calculated analytically within Comsol. Meshes representing such volumes were also developed within Comsol. Because tissue surfaces relatively close to the heated region were exposed to air in the cases monitored with MRTI, a heat flux with $h = 10.5$ W/m/°C [58, 59] and $T_f = 22$°C was used on the outer boundaries. Due to the complexity of tracing the paths of reflected and refracted rays through the irregular geometries of bone/muscle interfaces as required for Model A, these two cases were modeled using Models B-D.

Results

THEORY

Comparison of models in perfused tissue—Figure 4 shows the temperature maps predicted by Model B and compares the 240 CEM43°C contours, which correspond to ablated regions, for the four models when the applicator is placed in perfused muscle at 1 and 2 cm from a flat bone surface. The approximations in Models B and D produced thermal dose contours that closely matched the more comprehensive Model A. However, when the applicator was close enough to ablate the bone surface, Model C produced 240 CEM43°C contours that did not extend as deeply (5.0 mm) into the bones as the other three (5.3-5.8 mm). The boundary models (C and D) had significantly shorter computation times than the volumetric models (A and B). Model D was solved 3.6, 2.6, and 1.5 times faster than Models A, B, and C, respectively, when the applicator was 1 cm from bone. It took 218, 156, 89, and 60 minutes, respectively, to compute ten-minute transient simulations using Models A-D on an Intel Xeon X5680 processor. In these cases, Models C and D had a mesh size of 0.8 mm on the heated portion of the bone surface and 332,741 elements total, while Models A and B, which required a finer bone mesh, had a mesh size of 0.5 mm on heated bone surfaces and 540,505 elements total.

Parametric investigations—A parametric study was performed to investigate the influence of attenuation and perfusion on the volume of tissue that could be ablated in the presence of bone and to determine how the models perform in tissues with various properties. The maximum distance between the applicator and a flat bone at which all tissue between the two could be ablated is shown in Figure 5 for various soft tissue perfusions and attenuations. The maximum tumor size that could be ablated with zero and maximum perfusion in soft tissue without bone present is also shown.

Significantly larger tumors could be ablated when bone was present at the outer boundary, especially when the tumor attenuation was low. The largest tumors that could be ablated with bone present had low attenuations and perfusions, though there was a falloff in the volume that could be ablated at the lowest attenuations. At 13 kg/m^3/s and exceptionally low attenuation (3 Np/m/MHz), the combined effects of perfusion, low absorption, and catheter cooling for the parameters tested herein resulted in reduced heating in the tissue immediately adjacent to the applicator, so it could not be ablated within 10 minutes at the maximum allowable power unless bone was present. In practice, the cooling flow could be applied at a higher temperature or turned off immediately after power application to effectively coagulate tissue adjacent to the applicator. The four models agreed well on the radii of the ablated volumes, regardless of the tumor attenuation or perfusion, with better agreement at high attenuations. The discrepancy between the calculations made by Model A and the calculations made by the other models of the maximum distance between the bone and applicator at which all intervening tissue could be ablated was less than 2.6% for all cases evaluated.

EXPERIMENTS

***Thermal lesions:* Ex vivo *bone and tissue studies*—**Porcine muscle was ablated using interstitial ultrasound in a 37°C water bath, with the applicator positioned various distances from flat slabs of cortical and cancellous bone. Models A-D predicted coagulated regions of similar sizes and shapes as those produced experimentally (Figure 6). Model C tended to slightly underestimate the size of thermal lesions compared to the other models. The measurement of the distance between the applicator and the bone recorded after the ablation was consistently lower, particularly at higher powers, than the measurement from before the ablation by an average of 2.3 mm, which is attributed to tissue shrinkage during coagulation [60].

***Thermometry:* Ex vivo *bone and phantom studies*—**Figure 7 shows a series of temperature profiles measured in one phantom containing a rib bone (A) and another phantom containing cancellous bone (B) after 10 minute ablations by applicators positioned 5-30 mm from the bone/phantom interface. The temperatures were measured by thermocouples along a line running through the bone, into the phantom, and alongside one transducer (Figure 3B). The experiments were modeled, and the theoretical results created using the constant transmission volumetric model (Model B) are superimposed in Figure 7. The temperature peaked near the applicator, and a secondary peak or inflection was observed at the bone surface, behind which the temperature would sharply drop off. When the bone was within 1 cm of the applicator, the primary and secondary peaks overlapped, producing a single, higher temperature peak. The simulated models A-D demonstrated all of these trends in temperature.

The maximum temperature rises recorded after a 10 minute ablation are plotted against the distance between the applicator and the bone surface for each of the 40 trials in Figure 8A, with simulated data superimposed. Figure 8B shows the recorded and simulated temperature rises at the bone surface for each trial. The maximum temperature achieved tends to be constant with respect to applicator location until the applicator is within 1 cm from the bone, at which point the primary and secondary temperature peaks overlap, and the maximum temperature increases sharply. Overall the simulations predicted the maximum temperatures fairly accurately and reproduced the same trends as experiments. Some deviations between the two were observed, in that the simulations underestimated bone surface temperatures when the applicator was 15 mm or more from the bone, and over-predicted bone surface temperatures when the applicator was 5 mm from the bone.

Figure 9 shows the mean measured temperature profiles from experiments compared to simulated temperature profiles corresponding to each of the four models, for two example cases with the applicator 10 and 25 mm from cortical bone. Good agreement was observed between the experimental temperature profiles and simulations with Models A-D for all six distances between the applicator and the bone, with correlation coefficients ranging between 0.852 to 0.967 (Table III). The maximum p-value, based on a t-statistic, was 1.9e-31. The correlation coefficients between Model A and Models B-D were at least 0.995 for all six applicator locations, with maximum p-values, based on a t-statistic, of zero.

MR temperature imaging—The FEM meshes created based on segmented MR images captured the applicator position and the complex geometry of the soft tissues, bovine rib, and bovine vertebrae heated under MRTI monitoring (Figure 10). Parametric studies with complex geometries based on segmented MR images as well as simple geometries based on the phantom setup indicated that a 0.3-1 mm mesh was necessary on heated portions of the bone surface when using Models A and B, depending on the distance between the applicator and the bone, while a 0.8-1 mm mesh on heated bone surfaces was sufficient for Models C and D. The total mesh sizes and computation times for the rib models were 413,000 elements and 47 minutes for Model B, and 350,000 elements and 32-36 minutes for Models C and D. For the vertebra case, the simulations performed with Model B had 802,000 elements and took 85 minutes, while simulations using Models C and D had 428,000 elements and both took 49 minutes. These ten-minute-long transient simulations were performed on an Intel Xeon X5680 processor.

Figures 11-12 show the recorded temperature increases and simulated temperature contours 5 minutes into the ablation, when all soft tissue between the applicator and the bone was heated at least 15°C, which is ablative under *in vivo* conditions [54]. The predictions of the temperatures, as well as the shapes and sizes of the isothermal contours, produced by Models B and D were in close agreement with MRTI. Model C produced the smallest contoured areas, and Model B produced the largest. In the muscle surrounding the vertebrae in a 24 × 33 × 30 mm region around the transducers, the temperatures produced after a 10 minute ablation by Model B had an error of 0.1±4.0°C (mean ± standard deviation), Model C had an error of −1.2±3.8°C, and Model D had an error of −0.1±3.9°C when compared to experimental measurements. In the muscle surrounding the rib in a 24 × 37 × 30 mm region around the transducers, the temperatures produced by Model B had an error of −1.3±3.9°C (mean ± standard deviation), Model C had an error of −2.3±3.8°C, and Model D had an error of −1.4±3.8°C as compared to experimental measurements. The deviation of the models from experimental values was less significant at earlier time points. The models under-predicted the mild temperature rises experimentally observed behind the applicator, which is not heated by incident ultrasound energy, with errors less than or equal to the errors in the zone of maximal heating. Generally, lower errors in simulated temperatures were observed in the periphery, away from the zone of maximal heating. Tissue heterogeneity and the limitations of the slice thickness in MR images could possibly contribute to these errors.

Discussion

The presence of bone within or adjacent to a target region can dramatically influence the heating characteristics of ultrasound therapy in general, and specifically interstitial ultrasound as addressed in this study. Bone interfaces are complicated by two distinct parameters: high acoustic absorption of bone and high acoustic impedance differences. Bone has an ultrasound absorption coefficient 1-2 orders of magnitude higher than that of soft tissue [27], causing preferential heating at the bone surface [25, 28], effectively creating a secondary heat source and insulating structures behind the bone (Figures 6-7). Acoustic impedance differences between bone and soft tissue soft tissue result in reflection, refraction, and mode conversion at the interface, which complicate wave propagation and prediction of resultant heating patterns. Complex accurate acoustic modeling of this interface is computationally intensive and difficult, especially considering that the stress tensor in solids cannot be simplified as a one dimensional pressure as it can be in liquids. In this work we have devised approximate models of the interactions of interstitial ultrasound with bone. Theoretical and comparative experimental studies with bone/tissue phantoms and *ex vivo* tissues have demonstrated that these simplifications can provide accurate estimations of temperature distributions with reduced modeling complexity and computational requirements, and that they are practical for applications in treatment planning and modeling.

Models using four methods (A-D) of decreasing complexity to calculate heat deposition in bone were developed and compared. Models B and D produced temperature and thermal dose distributions very similar to the more comprehensive Model A (Figures 4-6, 9), demonstrating that neither angle-dependent nor volumetric heat sources are crucial to modeling high-frequency interstitial ultrasound heating in bone. Any discrepancies between the four models generally occurred near the most heated portions of the bone surface (Figures 4 and 9) and were lower at earlier time points. Model A, which included reflection, produced slightly higher temperatures in volumes of the soft tissue that are not heated by incident ultrasound energy than the other models (Figure 9). At 7 MHz, 69% (longitudinal) to 83% (shear) of the acoustic energy entering bone is attenuated and absorbed within 1 mm, and 97% (longitudinal) to 99.5% (shear) is absorbed within 3 mm. Shear and longitudinal penetration beyond 3 mm is negligible. Unless the bone is very thin, the amount of energy that exits the bone to propagate through soft tissue, which is further decreased by the transmission coefficient, is negligible and does not need to be modeled. The high attenuation coefficient of bone allows for so little acoustic penetration that the different pathways of shear and longitudinal waves do not need to be modeled separately, and heating can be approximated as occurring on the face of the bone surface.

The angle-dependent boundary model (C), however, consistently produced temperature distributions that were lower overall than the 3 other models and MRTI data (Figures 4, 6, 9, 11, 12). In regions with measured temperature increases over 15°C, Model C produced temperature increases 3.1±3.5% (mean ± standard deviation) below those of Model A in phantoms and 6.9±13.2% below those of thermocouple measurements in phantoms. The low heating observed in Model C may have resulted from the use of lower transmission and attenuation coefficients near normal incidence than Models B and D, as well as from neglecting the heat generated by reflected waves. When constant transmission coefficients are used (Models B and D), the lack of reflected energy resulted in only a slight decrease in soft tissue temperatures as compared to Model A (Figure 9).

Although Model D included the most approximations, it performed very well. Model D approximated Model A (the most comprehensive model) more closely than Models B and C did in almost all locations over a few millimeters away from the bone/phantom interface when the applicator was 1-3 cm away from it (Figure 9). The RMS (root mean square) errors in Models A-C, as compared to experimentally measured values in regions heated at least 5°C in phantoms, were each within 0.5°C of the RMS error of Model D. Also, Model D was much better than Model C and just slightly worse than Model B in estimating temperature measurements made by MRTI, with the applicator 5-10 mm from the bone surfaces.

Models A, B, and D are all suitable for simulating interstitial ultrasound ablation involving bone. The volumetric models A and B, however, can require a much finer mesh size (0.3-1 mm) at the bone surface than the surface models C and D (0.8-1 mm), possibly because they may need a fine resolution to capture the rapid falloff in acoustic intensity behind the bone surface. This greatly increases computational time, particularly when the bone has a high surface area. A is also difficult to model in complex geometries, as the paths of reflected and refracted beams must be traced. Although development of a fast modeling platform is not a primary goal of this study, the impact of model approximations on computation time was analyzed in consideration of potential future treatment planning applications. Since Models A, B, and D yield similar temperature predictions, the simplest and fastest one would be best suited to treatment planning. As such, Model D may be the most practical method for accurately simulating interstitial ultrasound bone ablation, with Model B preferable in cases when the bone is less than 1-2 mm thick.

Simulations produced temperature profiles and ablated volumes that closely matched experimental data in size and shape (Figures 6-9, 11, 12). Simulated temperatures were very close to data measured with thermocouples and MRTI. The one exception was the over-prediction of peak temperatures in phantoms when the applicator was 5 mm from the bone surface. Thermocouple conduction artifacts, which smear heating along the multi-junction thermocouple wires, may have contributed to this discrepancy [61]. This artifact would be more pronounced when a large amount of heat is deposited in a small region, as in the 5 mm phantom case, lowering the measured temperatures below the actual temperatures. The predicted temperatures at the phantom/bone interface when the applicator was 10 mm or more away from the bone were generally within the range of experimental values (Figure 8). Figures 6-9, 11, and 12 show fairly good agreement of temperature and thermal dose profiles between the models and the experiments in the zones of maximal heating at the end of treatment. Discrepancies between the models and experiments were generally even smaller at earlier time points and in locations away from the zones of maximal heating.

The results of this study demonstrate the importance of modeling the interactions of interstitial ultrasound with bone, as preferential bone heating can dramatically impact heating and thermal dose profiles. Simulations and temperature measurements in phantoms indicate that when an applicator is within 1 cm of the bone surface, the temperature peaks at the bone surface and in the soft tissue overlap, creating a high, narrow peak near the bone surface (Figure 7). When the applicator is further from the bone, the secondary peak at the bone surface can widen the ablated region without significantly changing peak temperatures (Figures 7-8). This effect is more pronounced at low attenuations and perfusions, when ultrasound can penetrate further into the tumor to reach the bone and less of the absorbed energy is carried away by flowing blood (Figure 5). These results agree with those of Moros et al., who performed similar experiments using phantoms with bone inclusions and an external planar transducer to study hyperthermia at 1.0 and 3.3 MHz in superficial tissues above bone [62]. They found that increased heating near the bone surface can be significant, and can be used to enhance acoustic and thermal penetration into deep tissue regions directly over bone. These studies also corroborated extensive theoretical investigations [34, 37], which were employed in part for the development of our models herein.

Comparison with MRTI data shows that the simulations of irregularly shaped bones produced fairly accurate biothermal and acoustic models. MRI is highly useful for its ability to monitor heating and to create images on which 3D models for treatment planning can be based. MRTI measured temperature rises in the soft tissue adjacent to bone. MRTI data within bone measured with the PRF method is inaccurate because cortical bone has low water content and thus a low MR signal, because cancellous bone has a high fat content, and because fat suppression was not applied. Future applications may be able to use fat suppression or data in adjacent soft tissues to infer or predict bone temperatures. The system developed here for modeling interstitial ultrasound ablation involving bone could potentially be used to plan and monitor treatments in complex osseous anatomy such as the spine.

Conclusion

Models and experimental data showed that preferential heating at bone surfaces can cause higher temperature elevations or allow larger volumes to be ablated with interstitial ultrasound. Four types of biothermal and acoustic models of interstitial ultrasound ablation involving bone were developed, applying various approximations, and compared to experimental data. Three of the models produced temperature and thermal dose profiles very similar to those observed experimentally. Approximations that considered a constant transmission coefficient, heat sources applied to the bone/soft tissue boundary, no reflection, and no shear mode conversion represented heating in bone and soft tissues with good accuracy, while simplifying and speeding up simulations. Models generated for case-specific anatomy, incorporating finite element meshes representing the precise geometry of the tissues heated, made fairly accurate temperature predictions, as evidenced by favorable comparison with MRTI data. Modeling techniques developed here can be applied to treatment planning and optimization in a wide variety of tumors near or adjacent to bone.

Acknowledgments

We gratefully acknowledge support by the National Institutes of Health grant R44CA112852. This work is a collaboration between UCSF and Acoustic MedSystems supported by an SBIR (Small Business Industry Research) grant from the NIH. Dr. E. Clif Burdette is affiliated with Acoustic MedSystems, Inc., which has a commercial interest in interstitial ultrasound technology.

References

1. Coleman R. Metastatic bone disease: Clinical features, pathophysiology and treatment strategies. Cancer Treat Rev. 2001; 27:165–76. [PubMed: 11417967]
2. Mundy GR. Metastasis to bone: Causes, consequences and therapeutic opportunities. Nat Rev Cancer. 2002; 2:584–93. [PubMed: 12154351]
3. Howlander, N.; Noone, AM.; Krapcho, M.; Neyman, N.; Aminou, R.; Altekruse, SF., et al., editors. SEER Cancer Statistics Review, 1975-2009 (Vintage 2009 populations). National Cancer Institute; Bethesda, MD: 2012.
4. Klimo P Jr. Schmidt MH. Surgical management of spinal metastases. The Oncologist. 2004; 9:188–96. [PubMed: 15047923]
5. Callstrom MR, Charboneau JW, Goetz MP, Rubin J, Atwell TD, Farrell MA, et al. Image-guided ablation of painful metastatic bone tumors: A new and effective approach to a difficult problem. Skeletal Radiol. 2006; 35:1–15. [PubMed: 16205922]
6. Georgy BA. Metastatic spinal lesions: State-of-the-art treatment options and future trends. Am J Neuroradiol. 2008; 29:1605–11. [PubMed: 18566009]
7. Healey JH, Brown HK. Complications of bone metastases. Cancer. 2000; 88:2940–51. [PubMed: 10898338]
8. Schwab JH, Springfield DS, Raskin KA, Mankin HJ, Hornicek FJ. What's new in primary bone tumors. J Bone Joint Surg Am. 2012; 94:1913–9. [PubMed: 23079883]
9. Rosenthal D, Callstrom MR. Critical review and state of the art in interventional oncology: Benign and metastatic disease involving bone. Radiology. 2012; 262:765–80. [PubMed: 22357881]
10. Pinto CH, Taminiau AHM, Vanderschueren1 GM, Hogendoorn PCW, Bloem JL, Obermann WR. Technical considerations in CT-guided radiofrequency thermal ablation of osteoid osteoma: Tricks of the trade. Am J Roentgenol. 2002; 179:1633–42. [PubMed: 12438068]
11. Tins B, Cassar-Pullicino V, McCall I, Cool P, Williams D, Mangham D. Radiofrequency ablation of chondroblastoma using a multi-tined expandable electrode system: Initial results. Eur Radiol. 2006; 16:804–10. [PubMed: 16267666]
12. Schaefer O, Lohrmann C, Markmiller M, Uhrmeister P, Langer M. Combined treatment of a spinal metastasis with radiofrequency heat ablation and vertebroplasty. Am J Roentgenol. 2003; 180:1075–7. [PubMed: 12646458]
13. Nakatsuka A, Yamakado K, Maeda M, Yasuda M, Akeboshi M, Takaki H, et al. Radiofrequency ablation combined with bone cement injection for the treatment of bone malignancies. J Vasc Interv Radiol. 2004; 15:707–12. [PubMed: 15231884]
14. Liberman B, Gianfelice D, Inbar Y, Beck A, Rabin T, Shabshin N, et al. Pain palliation in patients with bone metastases using MR-guided focused ultrasound surgery: A multicenter study. Ann Surg Oncol. 2009; 16:140–6. [PubMed: 19002530]
15. Catane R, Beck A, Inbar Y, Rabin R, Shabshin N, Hengst S, et al. MR-guided focused ultrasound surgery (MRgFUS) for the palliation of pain in patients with bone metastases—preliminary clinical experience. Ann Oncol. 2007; 18:163–7. [PubMed: 17030549]
16. Gianfelice D, Gupta C, Kucharczyk W, Bret P, Havill D, Clemons M. Palliative treatment of painful bone metastases with MR imaging-guided focused ultrasound. Radiology. 2008; 249:355–63. [PubMed: 18695209]
17. Simon CJ, Dupuy DE, Mayo-Smith WW. Microwave ablation: Principles and applications. Radiographics. 2005; 25:S69–S83. [PubMed: 16227498]
18. Gangi A, Dietemann J, Gasser B, Mortazavi R, Brunner P, Mourou M, et al. Interstitial laser photocoagulation of osteoid osteomas with use of CT guidance. Radiology. 1997; 203:843–8. [PubMed: 9169714]
19. Callstrom MR, Atwell TD, Charboneau JW, Farrell MA, Goetz MP, Rubin J, et al. Painful metastases involving bone: Percutaneous image-guided cryoablation—Prospective trial interim analysis. Radiology. 2006; 241:572–80. [PubMed: 17057075]
20. Diederich CJ. Ultrasound applicators with integrated catheter-cooling for interstitial hyperthermia: Theory and preliminary experiments. Int J Hyperthermia. 1996; 12:279–97. [PubMed: 8926395]

21. Nau WH, Diederich CJ, Burdette EC. Evaluation of multielement catheter-cooled interstitial ultrasound applicators for high-temperature thermal therapy. Med Phys. 2001; 28:1525–34. [PubMed: 11488586]
22. Lafon C, Melodelima D, Salomir R, Chapelon JY. Interstitial devices for minimally invasive thermal ablation by high-intensity ultrasound. Int J Hyperthermia. 2007; 23:153–63. [PubMed: 17578339]
23. Deardorff DL, Diederich CJ, Nau WH. Control of interstitial thermal coagulation: Comparative evaluation of microwave and ultrasound applicators. Med Phys. 2000; 28:104–17. [PubMed: 11213915]
24. Nau WH, Diederich CJ, Stauffer PR. Directional power deposition from direct-coupled and catheter-cooled interstitial ultrasound applicators. Int J Hyperthermia. 2000; 16:129–44. [PubMed: 10763742]
25. Fujii M, Sakamoto K, Toda Y, Negishi A, Kanai H. Study of the cause of the temperature rise at the muscle-bone interface during ultrasound hyperthermia. IEEE Trans Biomed Eng. 1999; 46:494–504. [PubMed: 10230128]
26. Chan AK, Sigelmann RA, Guy AW. Calculations of therapeutic heat generated by ultrasound in fat-muscle-bone layers. IEEE Trans Biomed Eng. 1974; BME-21:280–4. [PubMed: 4837475]
27. Duck, F. Physical Properties of Tissue: A Comprehensive Reference Book. Academic Press Limited; London: 1990.
28. Hynynen K, DeYoung D. Temperature elevation at muscle-bone interface during scanned, focused ultrasound hyperthermia. Int J Hyperthermia. 1988; 4:267–79. [PubMed: 3290347]
29. Bossy E, Padilla F, Peyrin F, Laugier P. Three-dimensional simulation of ultrasound propagation through trabecular bone structures measured by synchrotron microtomography. Phys Med Biol. 2005; 50:5545–56. [PubMed: 16306651]
30. Kaufman JJ, Luo G, Siffert RS. Ultrasound simulation in bone. IEEE Trans Ultrason, Ferroelectr, Freq Control. 2008; 55:1205–18. [PubMed: 18599409]
31. Behnia S, Jafari A, Ghalichi F, Bonabi A. Finite-element simulation of ultrasound brain surgery: Effects of frequency, focal pressure, and scanning path in bone-heating reduction. Cent Eur J Phys. 2008; 6:211–22.
32. Burtnyk M, Chopra R, Bronskill M. Simulation study on the heating of the surrounding anatomy during transurethral ultrasound prostate therapy: A 3D theoretical analysis of patient safety. Med Phys. 2010; 37:2862–75. [PubMed: 20632598]
33. Wootton JH, Ross AB, Diederich CJ. Prostate thermal therapy with high intensity transurethral ultrasound: The impact of pelvic bone heating on treatment delivery. Int J Hyperthermia. 2007; 23:609–22. [PubMed: 18097849]
34. Moros EG, Straube WL, Myerson RJ, Fan X. The impact of ultrasonic parameters on chest wall hyperthermia. Int J Hyperthermia. 2000; 16:523–38. [PubMed: 11129263]
35. Lin W-L, Liauh C-T, Chen Y-Y, Liu H-C, Shieh M-J. Theoretical study of temperature elevation at muscle/bone interface during ultrasound hyperthermia. Med Phys. 2000; 27:1131–40. [PubMed: 10841420]
36. Sun J, Hynynen K. Focusing of therapeutic ultrasound through a human skull: A numerical study. J Acoust Soc Am. 1998; 104:1705–15. [PubMed: 9745750]
37. Moros EG, Fan X, Straube WL. Ultrasound power deposition model for the chest wall. Ultrasound Med Biol. 1999; 25:1275–87. [PubMed: 10576270]
38. Wu J, Du G. Temperature elevation generated by a focused Gaussian ultrasonic beam at a tissue-bone interface. J Acoust Soc Am. 1990; 87:2748–55. [PubMed: 2197307]
39. Lu B-Y, Yang R-S, Lin W-L, Cheng K-S, Wang C-Y, Kuo T-S. Theoretical study of convergent ultrasound hyperthermia for treating bone tumors. Med Eng Phys. 2000; 22:253–63. [PubMed: 11018457]
40. Pennes HH. Analysis of tissue and arterial blood temperatures in the resting human forearm. J Appl Physiol. 1948; 1:93–122. [PubMed: 18887578]
41. Prakash P, Diederich CJ. Considerations for theoretical modelling of thermal ablation with catheter-based ultrasonic sources: Implications for treatment planning, monitoring and control. Int J Hyperthermia. 2012; 28:69–86. [PubMed: 22235787]

42. Sapareto SA, Dewey WC. Thermal dose determination in cancer therapy. Int J Radiat Oncol Biol Phys. 1984; 10:787–800. [PubMed: 6547421]
43. Diederich CJ, Hynynen K. Induction of hyperthermia using an intracavitary multielement ultrasonic applicator. IEEE Trans Biomed Eng. 1989; 36:432–8. [PubMed: 2714822]
44. Tyréus PD, Diederich CJ. Theoretical model of internally cooled interstitial ultrasound applicators for thermal therapy. Phys Med Biol. 2002; 47:1073–89. [PubMed: 11996056]
45. Chen X, Diederich CJ, Wootton JH, Pouliot J, Hsu I-C. Optimisation-based thermal treatment planning for catheter-based ultrasound hyperthermia. Int J Hyperthermia. 2010; 26:39–55. [PubMed: 20100052]
46. Wootton JH, Prakash P, Hsu I-CJ, Diederich CJ. Implant strategies for endocervical and interstitial ultrasound hyperthermia adjunct to HDR brachytherapy for the treatment of cervical cancer. Phys Med Biol. 2011; 56:3967. [PubMed: 21666290]
47. Prakash P, Salgaonkar VA, Clif Burdette E, Diederich CJ. Multiple applicator hepatic ablation with interstitial ultrasound devices: Theoretical and experimental investigation. Med Phys. 2012; 39:7338–49. [PubMed: 23231283]
48. Cheeke, JDN. Fundamentals and Applications of Ultrasonic Waves. CRC Press; Boca Raton, FL: 2012.
49. Riekkinen O, Hakulinen M, Timonen M, Töyräs J, Jurvelin J. Influence of overlying soft tissues on trabecular bone acoustic measurement at various ultrasound frequencies. Ultrasound Med Biol. 2006; 32:1073–83. [PubMed: 16829321]
50. Hakulinen MA, Day JS, Töyräs J, Timonen M, Kröger H, Weinans H, et al. Prediction of density and mechanical properties of human trabecular bone in vitro by using ultrasound transmission and backscattering measurements at 0.2-6.7 MHz frequency range. Phys Med Biol. 2005; 50:1629–42. [PubMed: 15815086]
51. Vaupel P, Kallinowski F, Okunieff P. Blood flow, oxygen and nutrient supply, and metabolic microenvironment of human tumors: A review. Cancer Res. 1989; 49:6449–65. [PubMed: 2684393]
52. Gerweck LE. Hyperthermia in cancer therapy: The biological basis and unresolved questions. Cancer Res. 1985; 45:3408–14. [PubMed: 3893686]
53. Dewey WC. Arrhenius relationships from the molecule and cell to the clinic. Int J Hyperthermia. 1994; 10:457–83. [PubMed: 7963805]
54. Kinsey AM, Diederich CJ, Rieke V, Nau WH, Butts Pauly K, Bouley D, et al. Transurethral ultrasound applicators with dynamic multi-sector control for prostate thermal therapy: In vivo evaluation under MR guidance. Med Phys. 2008; 35:2081–93. [PubMed: 18561684]
55. King RL, Liu YL, Maruvada S, Herman BA, Wear KA, Harris GR. Development and characterization of a tissue-mimicking material for high intensity focused ultrasound. IEEE Trans Ultrason, Ferroelectr, Freq Control. 2011; 58:1397–405. [PubMed: 21768024]
56. Rieke V, Butts Pauly K. MR thermometry. J Magn Reson Imaging. 2008; 27:376–90. [PubMed: 18219673]
57. Roujol S, Ries M, Quesson B, Moonen C, Denis de Senneville B. Real-time MR-thermometry and dosimetry for interventional guidance on abdominal organs. Magn Reson Med. 2010; 63:1080–7. [PubMed: 20373409]
58. Buccella C, De Santis V, Feliziani M. Prediction of temperature increase in human eyes due to RF sources. IEEE Trans Electromagn Compat. 2007; 49:825–33.
59. Wang J, Fujiwara O. FDTD computation of temperature rise in the human head for portable telephones. IEEE Trans Microw Theory Techn. 1999; 47:1528–34.
60. Brace CL, Diaz TA, Hinshaw JL, Lee FT. Tissue contraction caused by radiofrequency and microwave ablation: A laboratory study in liver and lung. J Vasc Interv Radiol. 2010; 21:1280–6. [PubMed: 20537559]
61. Dickinson RJ. Thermal conduction errors of manganin-constantan thermocouple arrays. Phys Med Biol. 1985; 30:445.
62. Moros EG, Novak P, Straube WL, Kolluri P, Yablonskiy DA, Myerson RJ. Thermal contribution of compact bone to intervening tissue-like media exposed to planar ultrasound. Phys Med Biol. 2004; 49:869–86. [PubMed: 15104313]

63. Damianou C, Sanghvi N, Fry F. Dependence of ultrasonic attenuation and absorption in dog soft tissues on temperature and thermal dose. J Acoust Soc Am. 1997; 102:628–34. [PubMed: 9228822]
64. Werner J, Buse M. Temperature profiles with respect to inhomogeneity and geometry of the human body. J Appl Physiol. 1988; 65:1110–8. [PubMed: 3182480]
65. Williams LR, Leggett RW. Reference values for resting blood flow to organs of man. Clin Phys Physiol Meas. 1989; 10:187–217. [PubMed: 2697487]
66. Calttenburg R, Cohen J, Conner S, Cook N. Thermal properties of cancellous bone. J Biomed Mater Res. 1975; 9:169–82. [PubMed: 1176477]
67. McCarthy I. The physiology of bone blood flow: A review. J Bone Joint Surg Am. 2006; 88:4–9. [PubMed: 17079361]
68. Wu J, Cubberley F. Measurement of velocity and attenuation of shear waves in bovine compact bone using ultrasonic spectroscopy. Ultrasound Med Biol. 1997; 23:129–34. [PubMed: 9080625]

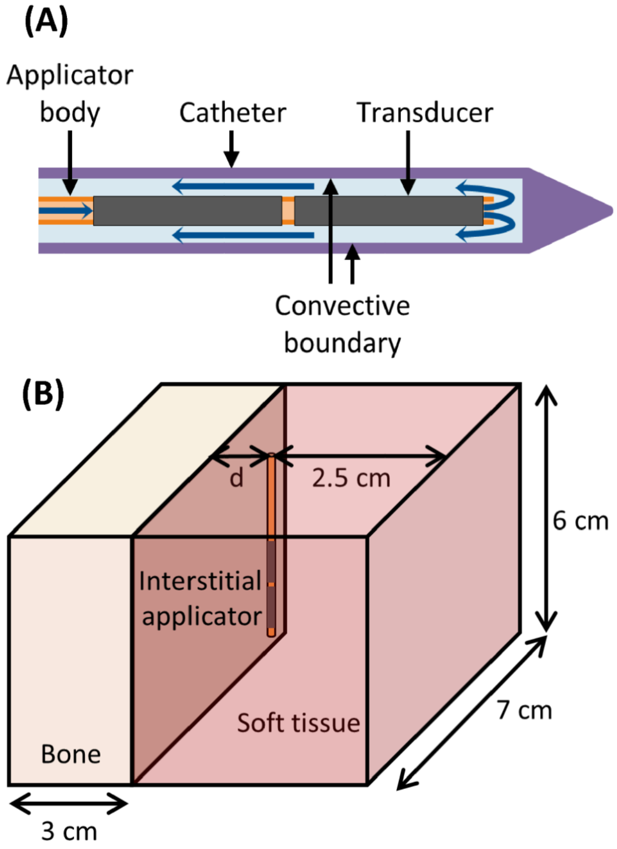

Figure 1.

(A) Diagram of the ultrasound applicators modeled. Blue arrows indicate the direction of cooling flow, which runs through the center of the applicator, out the tip, and then between the applicator and the catheter. Transducers have an outer diameter of 1.5 mm. The catheter has an outer diameter of 2.4 mm and an inner diameter of 1.89 mm. A convective boundary condition is applied to the inner wall of the catheter. (B) Geometry used to model interstitial ultrasound ablation with the applicator at various distances (0.5 cm < d < 3.2 cm) from the surface of a flat bone.

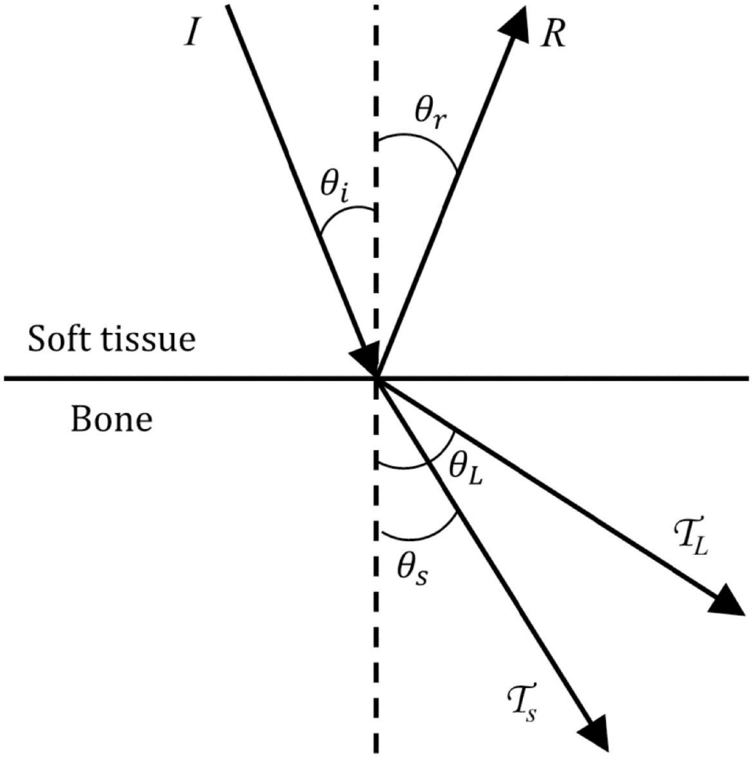

Figure 2.

Ultrasound reflection and refraction at bone/soft tissue interfaces, as used to derive the models herein. An incident wave strikes the bone surface at angle θ_i and intensity I. The reflected wave, refracted longitudinal wave, and refracted shear wave have intensities R, $\mathcal{T}_L$, and $\mathcal{T}_S$ and travel at angles, θ_r, θ_L and, θ_s respectively.

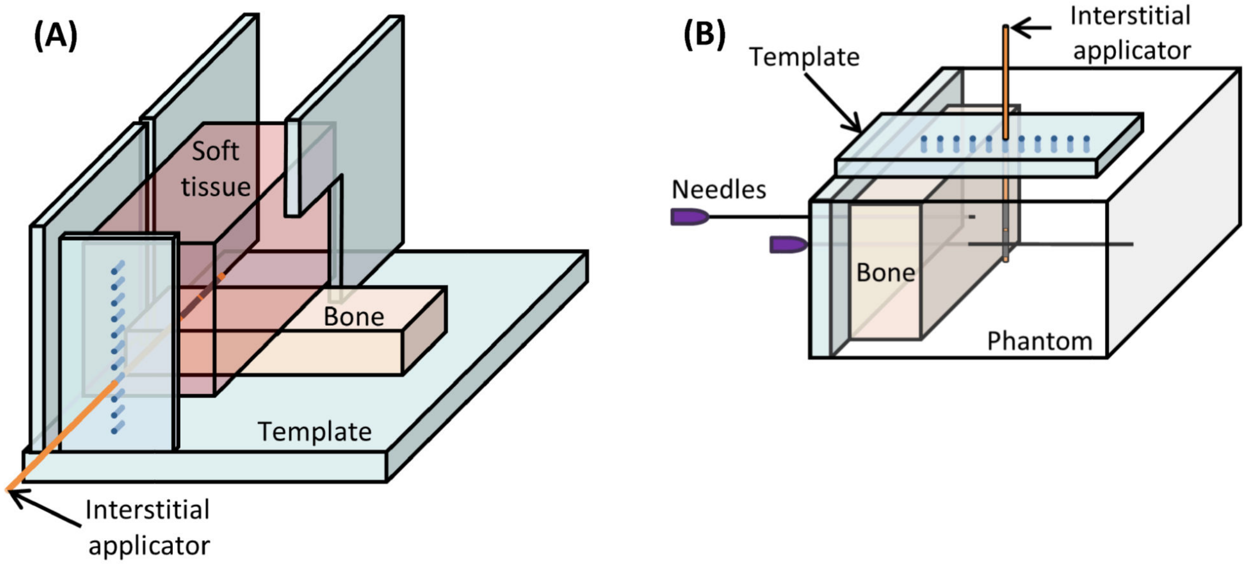

Figure 3.

Setup of *ex vivo* bench top experiments. (A) In experiments with *ex vivo* muscle and bone, a cut of porcine muscle was placed on top of bovine bone and heated. (B) In phantom and *ex vivo* bone experiments, the temperature rise in a phantom with an encapsulated bone was measured by thermocouples within needles.

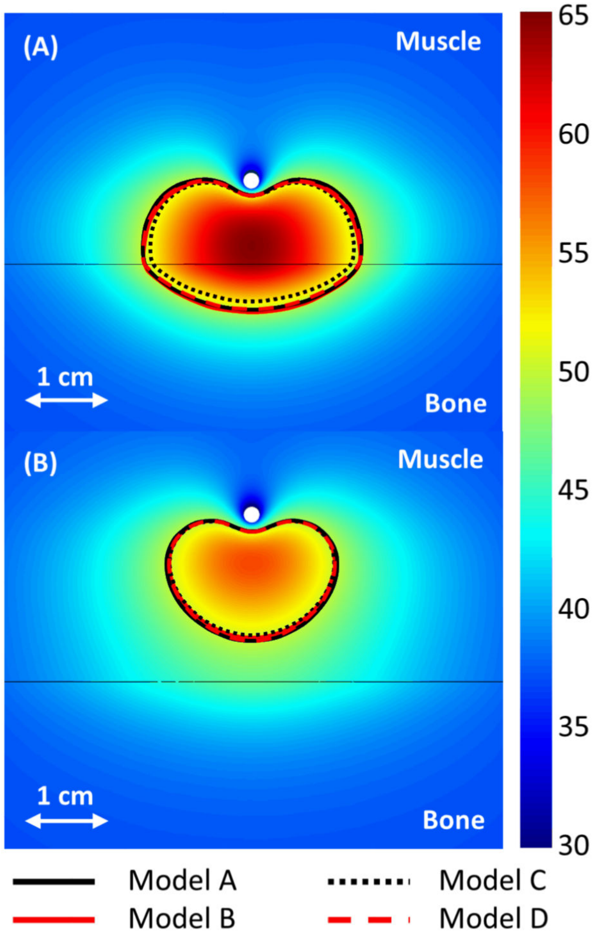

Figure 4.

240 CEM43°C contours calculated with Models A-D after a 10 minute ablation are shown in the central plane between the two transducers. The applicators (white circle) are placed 1 and 2 cm from a flat bone (black line) in A and B, respectively. A color map shows the temperatures (°C) calculated with the constant transmission volumetric model (Model B).

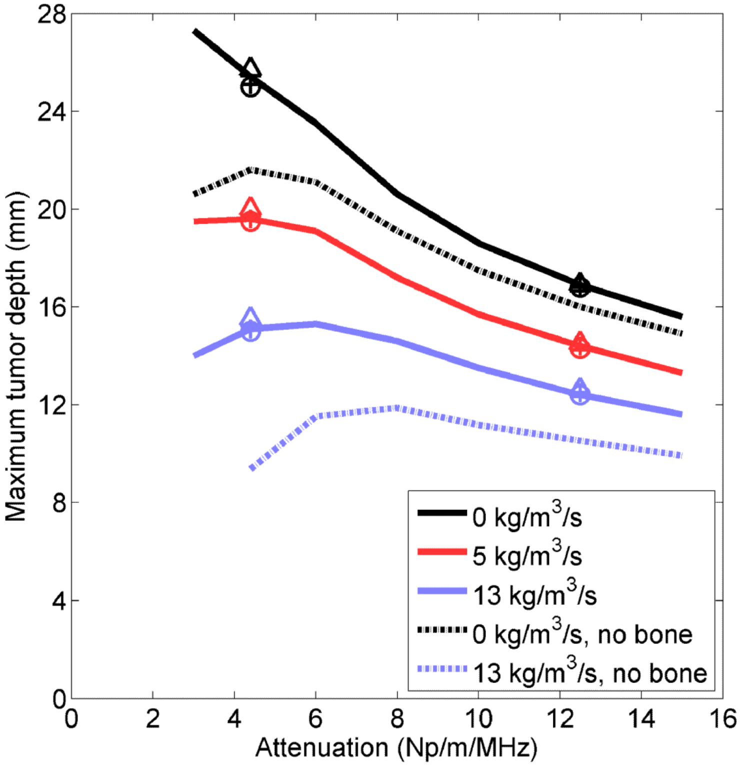

Figure 5.

The maximum distance between an applicator and a flat bone at which all tumor tissue between the two can be ablated within 10 minutes, given various ultrasound attenuations and blood perfusion rates in the tumor, as calculated by Model B. The maximum radius that can be fully ablated when bone is absent is also shown for 0 and 13 kg/m^3/s perfusion in the tumor. The maximum distance between an applicator and bone for which all intervening tissue can be ablated is also plotted for models A (+), C (o), and D (Δ) for attenuations of 4 and 12.5 Np/m/MHz and perfusions of 0 (black), 5 (red), and 13 (blue) kg/m^3/s.

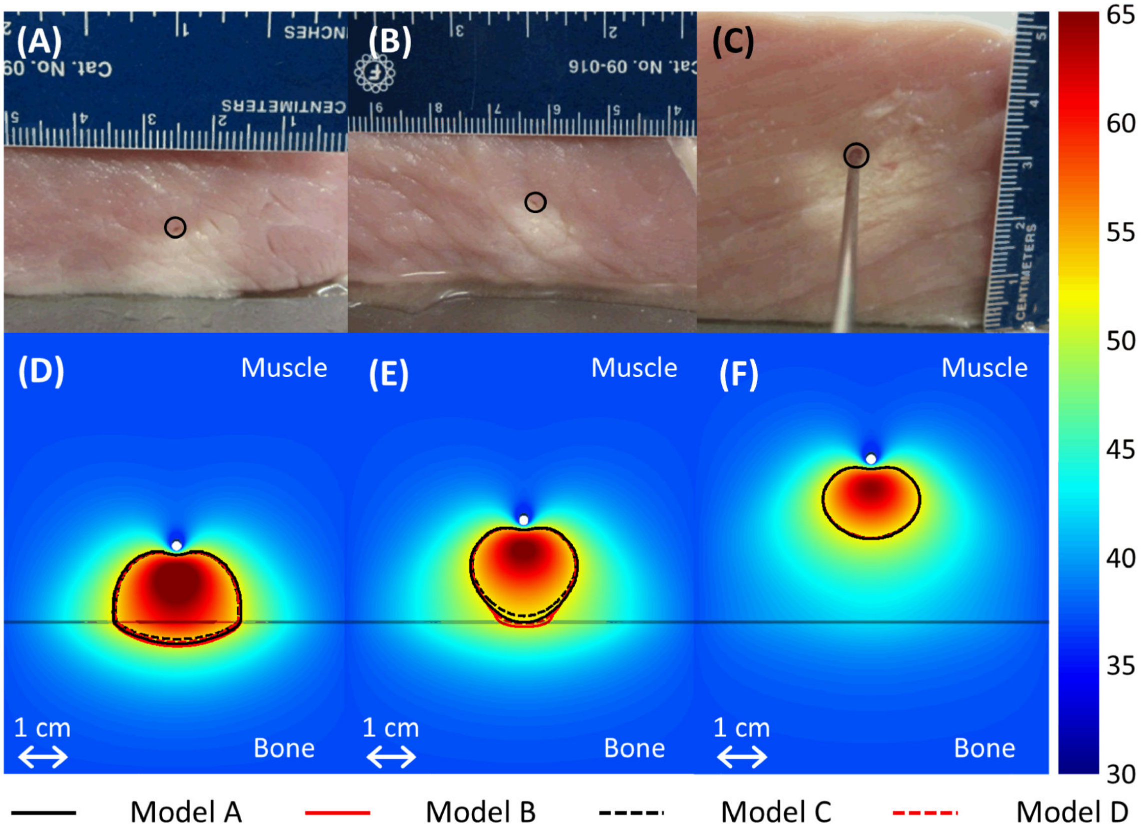

Figure 6.

(A-C) Thermal lesions created by 10 minute ablations at 12.5 acoustic W/cm^2 in porcine muscle positioned directly atop bovine bone, shown in central cross sections through the lesions. The catheter was measured as 15.2, 19.7, and 32.3 mm away from the bone before heating in A-C respectively, and 11.5, 17, and 32 mm away from the bone after the experiment. The catheter track is circled, and the side of the tissue that was against the bone is shown against the table. In C, a metal rod illustrates the catheter position. (D-F) The experiments were modeled with the applicator 15, 20, and 32 mm away from the bone, respectively, and the results after a 10 minute ablation are plotted in the central plane between the two transducers. The resulting temperature profiles produced by Model A are shown in a color map (°C). A black line indicates the bone/muscle boundary, and curves outline the 52°C temperature contours for Models A-D.

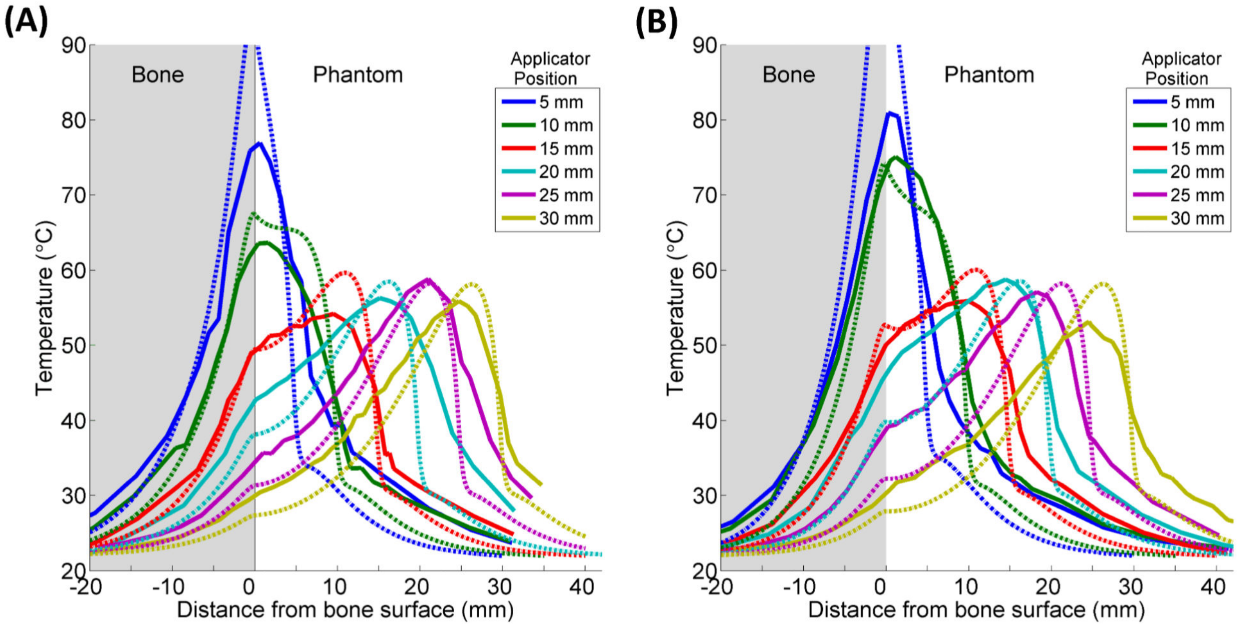

Figure 7.

Experimental (—) and simulated (- - -) temperature profiles after 10 minute ablations in two phantoms containing cortical (A) or cancellous (B) bone. Temperature along a line perpendicular to the bone surface and adjacent to the center of one transducer, as in Figure 3B, is plotted as a function of distance from the bone surface, which is at x = 0. Positive x-values are in the phantom, and negative values are inside the bone. Each solid curve corresponds to a single experimental trial with the applicator placed at the designated distance from the bone. The experiments were simulated with Model B, and the theoretical results are superimposed as dashed lines.

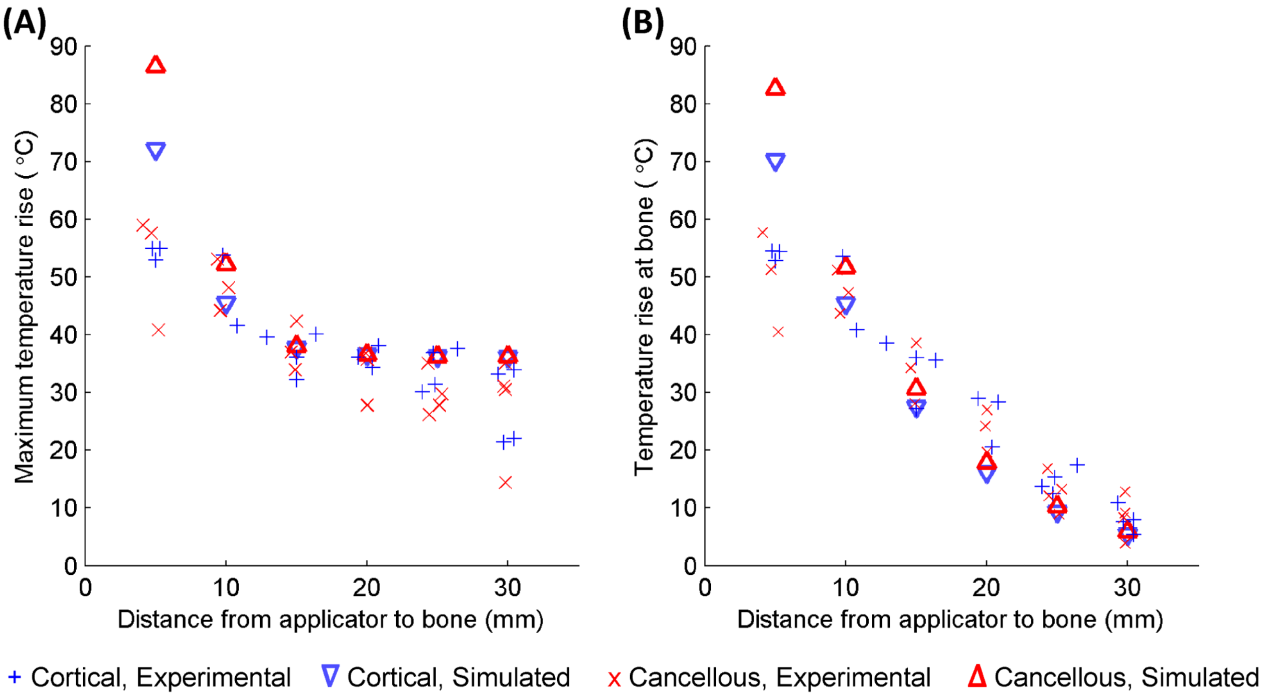

Figure 8.

The maximum temperature increase measured at the end of each 10 minute ablation of a phantom with an embedded bone is plotted in A. The temperature increase at the bone surface at the end of each trial is plotted in B. Peak (A) and bone (B) temperature increases produced by simulations using the constant transmission longitudinal model (Model B) are superimposed.

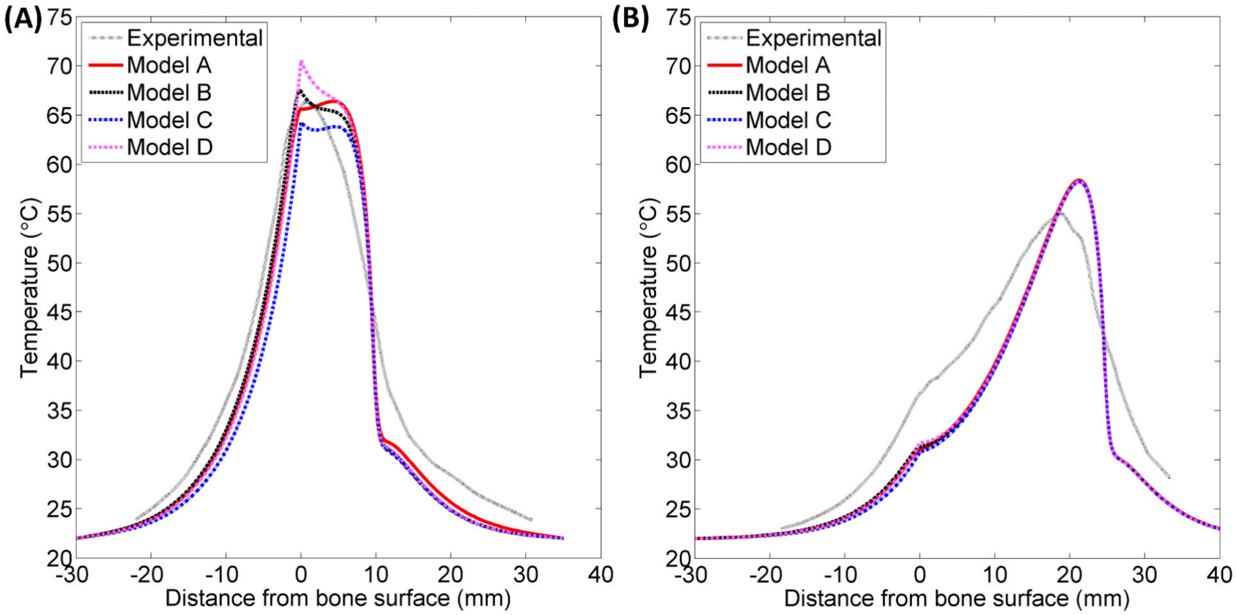

Figure 9.

Simulated and experimental temperature profiles in phantoms with an applicator placed 10 mm (A) and 25 mm (B) from a rib surface. Temperature along a line perpendicular to the bone surface and adjacent to the center of one transducer, as in Figure 3B, is plotted as a function of distance from the bone surface, which is at x = 0. Recordings were made after 10 minutes of heating. The experimental curve is an average of the recordings in 3-4 experiments with the applicator at the given position. The bone surface is at x = 0. Positive x-values indicate locations in the phantom, and negative values are inside the bone.

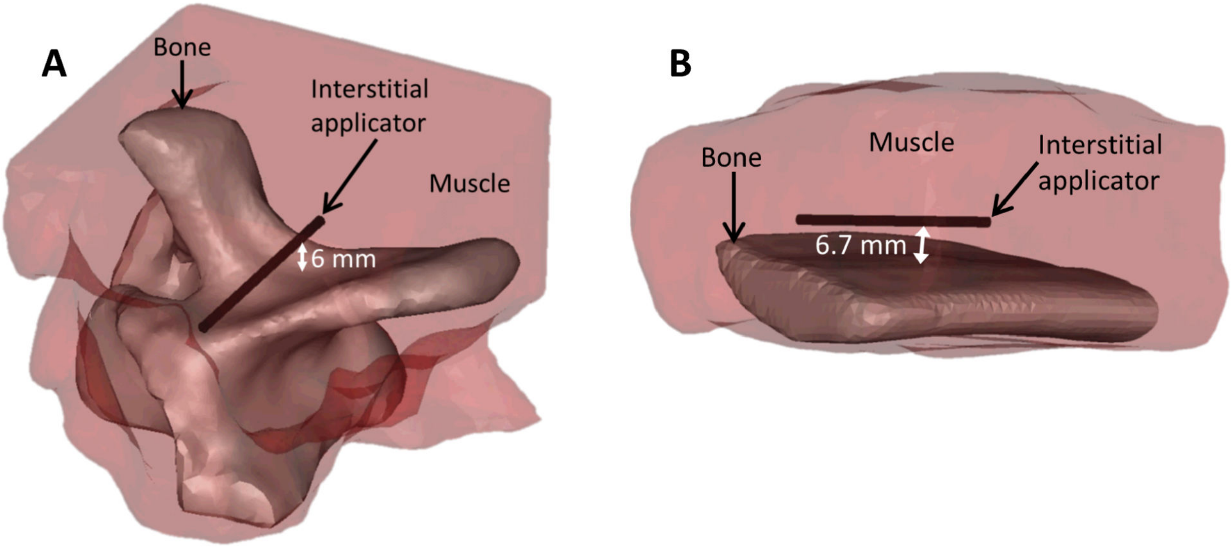

Figure 10.
3D objects that were meshed to model the bovine vertebra (A) and bovine rib (B) ablations monitored by MR thermometry.

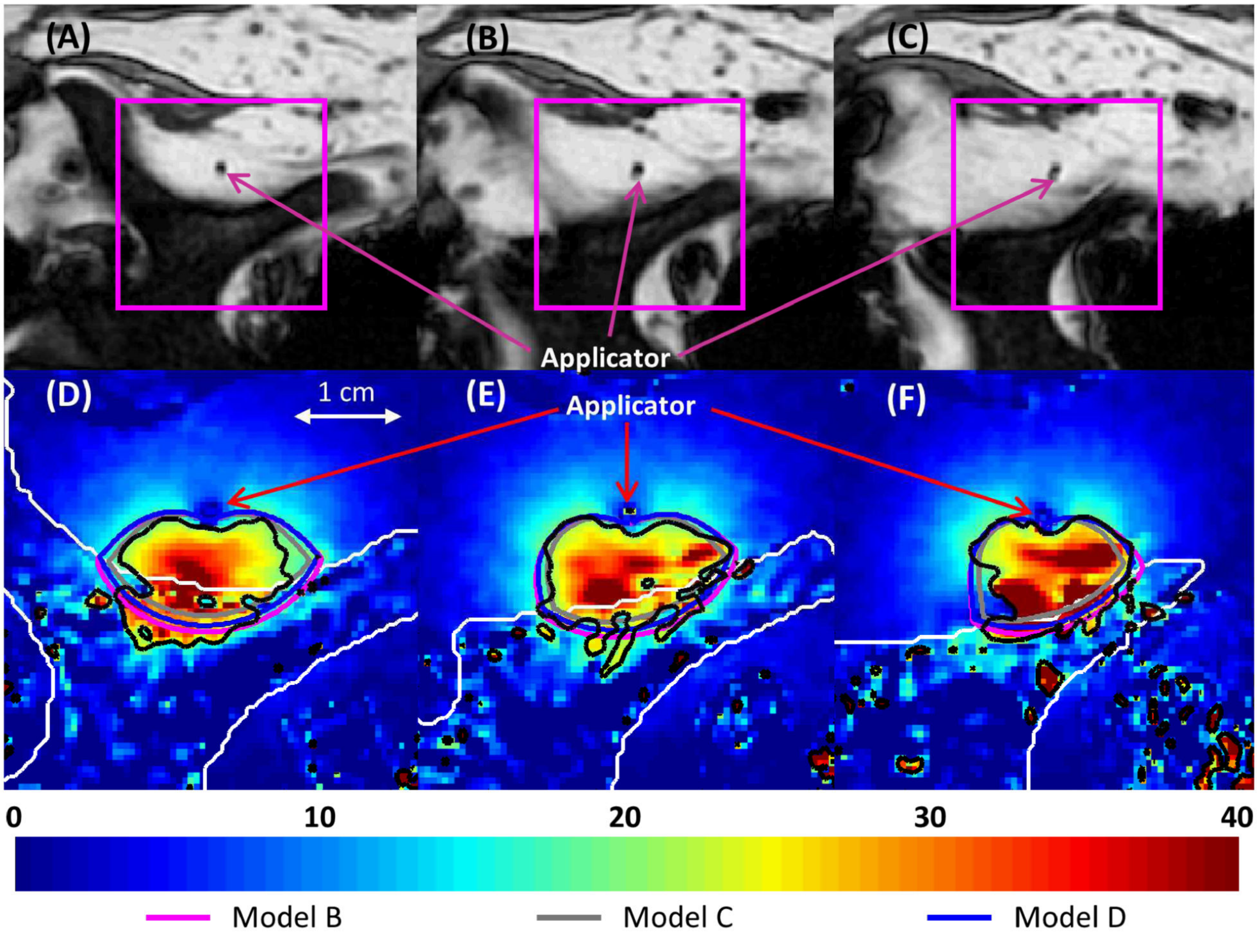

Figure 11.

(A-C) MR images of the 3 central heated axial slices of *ex vivo* bovine vertebrae, spaced 5 mm apart. (D-F) Color map of temperature increases (°C) recorded with MRTI in a smaller field of view (magenta box) for each slice 5 min into the ablation. Bone is outlined with a white line, and the 20°C temperature increase contours recorded by MRTI are outlined in black. Also shown are the simulated 20°C temperature increase contours produced by Models B (magenta), C (gray), and D (blue).

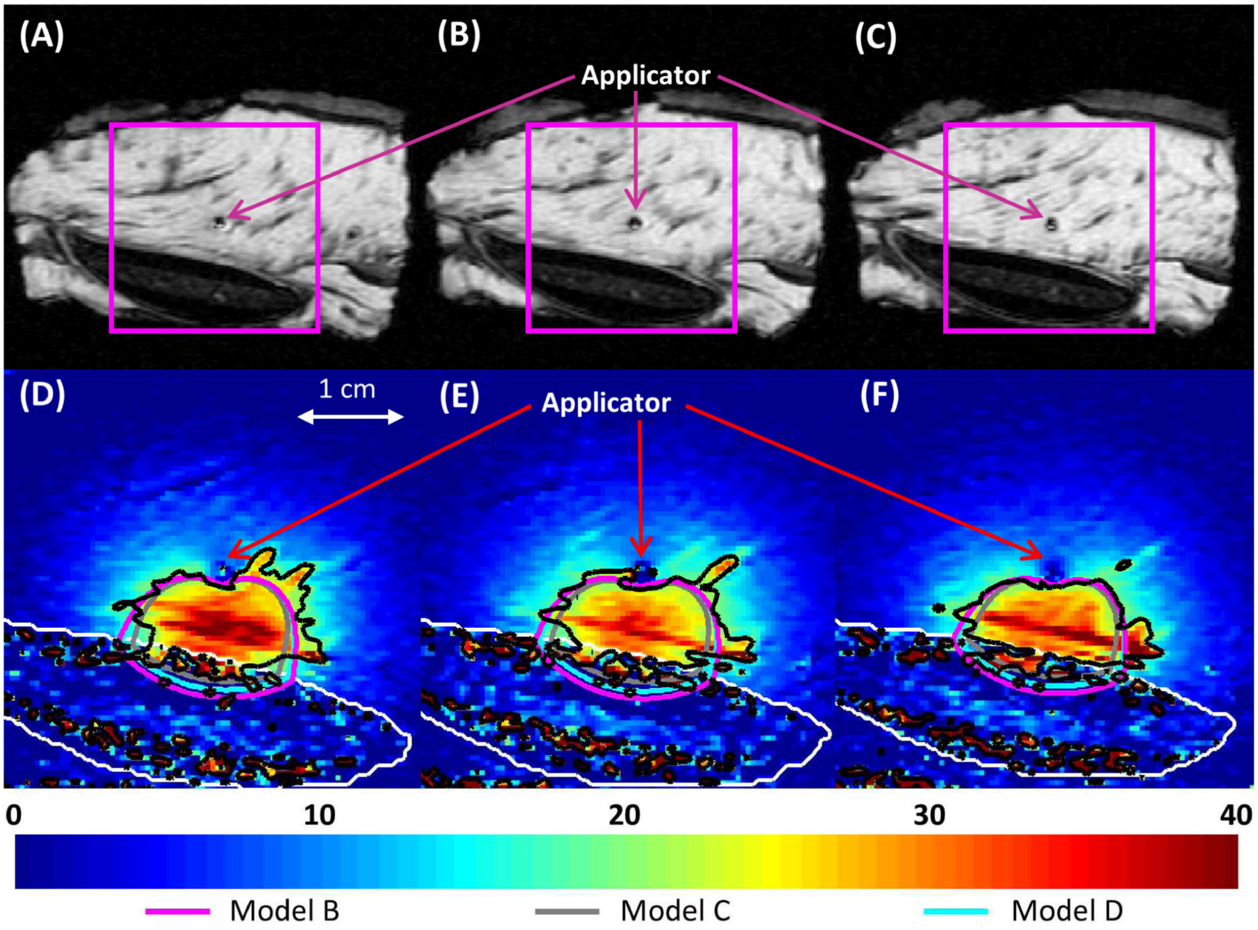

Figure 12.

(A-C) MR images of the 3 central heated axial slices of *ex vivo* bovine rib, spaced 5 mm apart. (D-F) Color map of temperature increases (°C) recorded with MRTI is shown in a smaller field of view (magenta box) for each slice 5 min into the ablation. Bone is outlined with a white line, and the 20°C temperature increase contours recorded by MRTI are outlined in black. Also shown are the 20°C temperature increase contours produced by Models B (magenta), C (gray), and D (cyan).

Table I

Material properties used in biothermal models.

Medium	**Density (kg/m^3)**	**Velocity (m/s)**	**Attenuation (Np/m/MHz)**	**Thermal conductivity (W/m/°C)**	**Specific heat (J/kg/°C)**	**Perfusion rate ($kg/m^3/s$)**[*]
Muscle	1041 [27]	1576 [27]	4.4 to 6.6, linearly increasing over 49.2 to 65°C[**] [63]	0.5 [27]	3430 [27]	0.692 [27]
Phantom	1030 [55]	1602 [55]	5.6 [55]	0.59 [55]	4900 [55]	0
Generic composite bone	1420 [27]	3260 [27]	105 [27]	0.38 [27]	1700 [64]	0.892 [65]
Cancellous bone	1080 [27]	2198 [50]	117.4 [50]	0.29 [66]	2828 [66]	3.78 [67]
Cortical bone	1990 [27]	3540 long 1770 shear [27, 68]	84 long 127 shear [68]			
Blood					3800 [27]	

[*] Perfusion was set to 0 when modeling bench top experiments.

[**] Temperature-dependence of muscle attenuation was considered when modeling *ex vivo* experiments performed at physiological temperatures. Otherwise, muscle attenuation was set to 5 Np/m/MHz.

Table II

Properties of the four types of models.

Model	A: Angle-dependent volumetric	B: Constant transmission volumetric	C: Angle dependent boundary	D: Constant transmission boundary
Bone heat source	Volume	Volume	Surface	Surface
Transmission coefficient	Angle-dependent	Constant	Angle-dependent	Constant
Shear mode conversion	Yes	No	Yes	No
Reflection	Yes	No	No	No
Refraction	Yes	No	No	No

Table III

Correlation coefficients between experimental and simulated temperature profiles in phantoms.

Distance between applicator and bone (mm)	**30**	**25**	**20**	**15**	**10**	**5**
Model A	0.854	0.893	0.886	0.901	0.955	0.967
Model B	0.853	0.892	0.888	0.908	0.960	0.958
Model C	0.852	0.890	0.878	0.889	0.944	0.961
Model D	0.853	0.893	0.890	0.907	0.955	0.958

The correlation coefficients between each of the 4 models A-D and the temperature measurements recorded at all thermocouple locations in 3-4 phantoms after a 10 minute ablation were calculated for each of the 6 applicator positions. The maximum p-value, based on a t-statistic, was 1.9e-31.